

An Efficient WENO-reconstruction-based high-order Gas-kinetic Scheme for Viscous Flows

Li-Jun Xuan, Kun Xu

*Mathematics Department,
Hong Kong University of Science and Technology
Clear Water Bay, Kowloon, Hong Kong*

Abstract

Based on the Weighted Essential Non-Oscillatory (WENO) reconstruction for the macroscopic flow variables and the direct use of the corresponding gas distribution function of the Navier-Stokes (NS) solution, a high-order finite volume gas-kinetic scheme is constructed. Different from the previous high-order gas-kinetic method [Li, Xu, and Fu, A high-order gas-kinetic Navier-Stokes solver, *J. Comput. Phys.*, 229 (2010) 6715-6731], which uses a discontinuous initial reconstruction at the cell interface, the present scheme is based on a continuous flow distribution. In the current study, in order to capture the discontinuities properly, the WENO reconstruction is combined with monotonicity preserving limiter in the initial data reconstruction. The space and time dependent multidimensional NS gas distribution function is used to evaluate the time-dependent interface flux function, which is further integrated along the cell boundary to get total mass, momentum, and energy transport within a time step. Since the Runge-Kutta time stepping method is not used here, the current scheme becomes highly accurate and efficient. With the same WENO reconstruction on characteristic variables, the current multidimensional finite volume gas-kinetic scheme is even more accurate and efficient than the well-defined finite difference WENO-JS scheme [Jiang and Shu, Efficient implementation of Weighted ENO schemes, *J. Comput. Phys.* 126 (1996) 202-228]. The numerical experiments also show that the current scheme is highly stable and non-oscillatory in capturing discontinuity.

Key Words: high-order finite volume gas-kinetic scheme, WENO reconstruction, monotonicity preserving limiter.

1. Introduction

Starting from a discontinuous initial reconstruction at a cell interface, the gas-kinetic schemes (GKS) have been constructed for compressible flow simulations [23, 24, 16]. Due to the flow variable

Email addresses: maljxuan@ust.hk (Li-Jun Xuan), makxu@ust.hk (Kun Xu)

jump at the interface, the gas evolution process in GKS covers the particle free transport to the Navier-Stokes solution construction, and the flow regime used for the flux evaluation depends on the ratio of time step Δt to the particle collision time τ . This gas evolution dynamics is different from the Riemann solution with the assumption of infinite number of particle collisions [10]. In GKS there is a smooth transition from upwind to central difference. The flux evaluation includes the effects from flow gradients explicitly in both normal and tangential directions at a cell interface, which makes the GKS be a multidimensional scheme [26, 14, 9]. The above GKS with discontinuous initial data is not very sensitive to the initial data reconstruction, because the numerical dissipation is included in the scheme through the initial discontinuity and the particle free transport mechanism [24, 10]. Therefore, the conservative variables are directly used in the reconstruction. For the smooth flow and the low speed limit, the GKS can be much simplified [7, 25].

In this paper, we are going to use space and time dependent NS gas distribution function directly for the construction of a high order multidimensional finite volume GKS. As a direct extension of Xuan and Xu's (2012) [27] idea to high order scheme, which is different from the previous GKS methods [24, 12, 14], continuous macroscopic flow distributions at the cell interface are reconstructed through the upwind-biased interpolation of characteristic variables as the initial condition, and the kinetic formulation is used for their space and time evolution. In the initial reconstruction, a well-defined Weighted Essential Non-Oscillatory (WENO) interpolation [11, 8, 19] with Yamaleev and Carpenter's weight [28] is implemented in the scheme. The using of Yamaleev et. al's weight can increase the accuracy of the scheme in smooth region and make a sharp shock transition. Due to the use of smooth flow distribution at a cell interface, it is much more difficult to control the numerical dissipation in the current scheme. At strong shock cases, the above scheme constructed thereby is apt to blow up. Therefore, on this occasion, we also adopt the monotonicity preserving limiter (MP-limiter) given by Daru and Tenaud to stabilize the scheme [5]. Theoretically, the MP-limiter can preserve monotonicity in solving linear equation without losing the accuracy in smooth region. For solving non-linear equation, it can effectively suppress the numerical oscillation near discontinuity and prevent the scheme from blowing up. Starting from a continuous initial reconstruction, the time and space evolution of the corresponding NS gas distribution function is used for the flux evaluation. Due to the time accurate multidimensional gas evolution solution, the current GKS does not need to use Runge-Kutta time stepping method, and the space and time dependent flux can be directly integrated along a cell interface. Therefore, the current scheme is much more efficient than the previous GKS methods with discontinuous initial data. Based on the above construction, the current scheme is named MPWENO-GKS. The scheme without MP-limiter is named WENO-GKS.

In summary, the MPWENO-GKS has the following distinguishable features:

1. The MPWENO-GKS is a high order scheme, and the order of the scheme depends on the initial reconstruction.
2. Because of the application of a continuous initial condition and the direct use of the NS gas distribution function, the MPWENO-GKS is highly efficient. The current finite volume GKS is even faster than the finite difference WENO-JS method under the same order initial reconstruction

[8].

3. The application of Yamaleev et.al.'s weight and MP-limiter makes the scheme have a high resolution for capturing short waves and shock discontinuities with smaller oscillations, in comparison with the classical high order WENO-JS schemes for the macroscopic governing equations directly.
4. The direct use of a multidimensional time dependent gas distribution function for the flux evaluation and boundary integration makes the scheme be easily extended to unstructured meshes once an appropriate high-order initial reconstruction scheme can be used.
5. The use of a continuous flow distribution at the cell interface may reduce the robustness of the current scheme in comparison with previous GKS methods following the evolution of a discontinuous initial data [24, 12, 9]. The current method is definitely more sensitive to the initial data reconstruction.

Many benchmark flow problems in one and two dimensions have been tested to validate current scheme. Our numerical experiments show that MPWENO-GKS is a highly stable, accurate, and efficient method, which presents excellent performance in capturing discontinuity.

The paper is arranged in the following. In section 2, the construction of GKS scheme is introduced. The fifth-order WENO interpolation with Yamaleev and Carpenter's weight [28] is presented in section 3. And a brief introduction of monotonicity preserving limiter is given in section 4. In section 5 many benchmark flow problems are computed and the results are compared with standard 5th-order finite difference WENO methods. The last section is the conclusion.

2. Construction of the scheme

2.1. One-dimensional scheme

Consider a mesh with $x_{i+1/2}$ ($i = 0, \dots, N$, N is the grid number) as the cell interfaces and cell center points $x_i = (x_{i-1/2} + x_{i+1/2})/2$ ($i = 1, \dots, N$). The Navier-Stokes gas distribution function $f(x, t, u, \xi)$ at any point in space and time (x, t) can be written as

$$f(x, t, u, \xi) = g(x, t, u, \xi) - \tau Dg(x, t, u, \xi), \quad (1)$$

where $g(x, t, u, \xi)$ is the equilibrium state distribution function, τ is the particle collision time, u is particle velocity, ξ is internal variable, and $D = \partial_t + u\partial_x$ ($\partial_\alpha \equiv \frac{\partial}{\partial \alpha}$). The deviation from the equilibrium state is controlled by the relaxation time τ , which is also a function of viscosity coefficient. The above NS distribution function can be obtained from the Chapman-Enskog expansion of the BGK model [2, 23].

After we know the NS gas distribution function at a point in space and time, we can get the corresponding distribution function nearby using the Taylor expansion in space and time. As the approach in [12, 14], around cell interface $x = x_{i+1/2}$ we can use the 3rd-order Taylor expansion to

approximate the equilibrium state $g(x, t, u, \xi)$,

$$\begin{aligned} g &= g^e \left\{ 1 + a_x x + a_t t + \frac{1}{2}[(a_x^2 + a_{xx})x^2 + (a_t^2 + a_{tt})t^2] + (a_x a_t + a_{xt})xt \right\} \\ &= g^e \left[1 + a_x x + a_t t + \frac{1}{2}(A_{xx}x^2 + A_{tt}t^2) + A_{xt}xt \right], \end{aligned} \quad (2)$$

where g^e is the initial Maxwellian equilibrium state at $(x = 0, t = 0)$ (assumed expansion point), and all other coefficients can be expressed as $A_{xx} = a_x^2 + a_{xx}$, $A_{tt} = a_t^2 + a_{tt}$, $A_{xt} = a_x a_t + a_{xt}$. Hence, the NS distribution function at (x, t) in (1) becomes

$$f = g^e \left\{ \begin{array}{l} 1 + a_x x + a_t t + \frac{1}{2}(A_{xx}x^2 + A_{tt}t^2) + A_{xt}xt \\ - \tau[u(a_x + A_{xx}x + A_{xt}t) + a_t + A_{xt}x + A_{tt}t] \end{array} \right\}, \quad (3)$$

where

$$a_x = a_{x,i}\psi_i, \quad a_t = a_{t,i}\psi_i, \quad a_{xx} = a_{xx,i}\psi_i, \quad a_{xt} = a_{xt,i}\psi_i, \quad a_{tt} = a_{tt,i}\psi_i, \quad (4)$$

where $\psi = [1, u, (u^2 + \xi^2)/2]^T$ and $\xi^2 = \xi_1^2 + \dots + \xi_K^2$. Here K is the total number of internal degrees of freedom. The repeating of subscript i means summation of i from 1 to 3.

From the values and derivatives of macroscopic conservative variables W_α ($\alpha = 1, 2, 3$) at a point in space and time, which will be obtained by WENO reconstruction method in the next section, the spatial derivatives in the distribution functions can be determined as (see [12]),

$$\begin{aligned} \langle a_x \rangle &= \frac{\partial W_\alpha}{\partial x}, \quad \langle A_{xx} \rangle = \frac{\partial^2 W_\alpha}{\partial x^2}, \\ \langle \cdot \rangle &\equiv \int g^e \cdot \psi_\alpha d\Xi, \end{aligned} \quad (5)$$

where $d\Xi = dud\xi$ is the volume element in the phase space with $d\xi = d\xi_1 d\xi_2 \dots d\xi_K$.

Based on the compatibility condition of the BGK model,

$$\langle f - g \rangle = 0, \quad (6)$$

we can derive the connections among the expansion coefficients [12],

$$\langle u a_x + a_t \rangle = 0, \quad \langle u A_{xx} + A_{xt} \rangle = 0, \quad \langle u A_{xt} + A_{tt} \rangle = 0, \quad (7)$$

from which a_t , a_{xt} , and a_{tt} can be solved. After the determination of one-dimensional distribution function $f(x, t, u, \xi)$ in (3), we can compute the flux $F(t)$ for the macroscopic variables at the cell interface

$$F(t) = \int u f \psi d\Xi = F^c(t) - F^v(t), \quad (8)$$

where $F^v(t) = \tau \int u Dg\psi d\Xi$ is viscous flux, such that

$$F^v(t) = \tau [\langle u^2 a_x \rangle + \langle u a_t \rangle + (\langle u^2 A_{xt} \rangle + \langle u A_{tt} \rangle) t], \quad (9)$$

and $F^c(t)$ is the Euler flux which will be calculated from the conservative variables $W(t)$ determined by $g(t)$, i.e.,

$$\begin{aligned} W(t) &= \int g\psi d\Xi = W^e + \langle a_t \rangle t + \langle A_{tt} \rangle t^2 / 2, \\ F^c(t) &= [\rho U, \rho U^2 + p, (E + p)U]^T, \end{aligned} \quad (10)$$

in which ρ, U, E, p are the physical variables determined by $W(t)$ and W^e is the conservative variable corresponding to g^e at the location ($x = 0, t = 0$).

To get the numerical flux transport within a time step $\hat{F}_{i+1/2} = \int_{t^n}^{t^{n+1}} F(t) dt$, we chose two Gauss-Legendre points (t_{G1}, t_{G2}) in $[0, \Delta t = t^{n+1} - t^n]$ and calculate the corresponding F^c and F^v , then use Gauss quadrature to compute the time integral up to 3rd-order,

$$\hat{F}_{i+1/2} = \frac{\Delta t}{2} [F^c(t_{G1}) - F^v(t_{G1}) + F^c(t_{G2}) - F^v(t_{G2})]. \quad (11)$$

After these procedures the local conservative law is used to update the cell averaged conservative variables

$$\begin{aligned} \bar{W}_i^{n+1} &= \bar{W}_i^n - \frac{1}{\Delta x} \int_{t_n}^{t_{n+1}} [F(t, x_{i+1/2}) - F(t, x_{i-1/2})] dt \\ &= \bar{W}_i^n - \frac{\hat{F}_{i+1/2} - \hat{F}_{i-1/2}}{\Delta x}. \end{aligned} \quad (12)$$

2.2. Two-dimensional scheme

On a rectangular mesh with cell center $[x_i, y_j]$ ($i = 1, \dots, N; j = 1, \dots, M$), the central point of a cell interface $x = x_{i+1/2}, y \in [y_{j-1/2}, y_{j+1/2}]$ is $(x, y) = (x_{i+1/2}, y_j)$. To simplify the notation, ($x_{i=1/2} = 0, y_j = 0$) is assumed. Around this point, a 3^{rd} -order Taylor expansion of the equilibrium state distribution function becomes

$$g = g^e \left[1 + a_x x + a_y y + a_t t + \frac{1}{2} (A_{xx} x^2 + A_{yy} y^2 + A_{tt} t^2) + A_{xy} xy + A_{xt} xt + A_{yt} yt \right], \quad (13)$$

with $A_{yy} = a_y^2 + a_{yy}$, $A_{xy} = a_x a_y + a_{xy}$, $A_{yt} = a_y a_t + a_{yt}$, $a_x = a_{x,i} \psi_i, \dots$ ($i = 1, 2, 3, 4$) and $\psi = [1, u, v, (u^2 + v^2 + \xi^2)/2]$. Based on the NS gas distribution function $f(x, y, t, u, v, \xi)$ and $f = g - \tau Dg$, we have

$$f = g^e \left\{ \begin{aligned} &1 + a_x x + a_y y + a_t t + \frac{1}{2} (A_{xx} x^2 + A_{yy} y^2 + A_{tt} t^2) + A_{xy} xy + A_{xt} xt + A_{yt} yt \\ &- \tau [u(a_x + A_{xx} x + A_{xy} y + A_{xt} t) + v(a_y + A_{xy} x + A_{yy} y + A_{yt} t) \\ &+ a_t + A_{xt} x + A_{yt} y + A_{tt} t] \end{aligned} \right\}. \quad (14)$$

Again the spatial derivatives in (14) are determined by

$$\langle a_x \rangle = \partial_x W, \quad \langle a_y \rangle = \partial_y W, \quad \langle A_{xx} \rangle = \partial_{xx} W, \quad \langle A_{xy} \rangle = \partial_{xy} W, \quad \langle A_{yy} \rangle = \partial_{yy} W. \quad (15)$$

We can further determine other expansion coefficients from the compatibility condition (6) as

$$\begin{aligned} \langle ua_x + va_y + a_t \rangle &= 0, \quad \langle uA_{xx} + vA_{xy} + A_{xt} \rangle = 0, \\ \langle uA_{xy} + vA_{yy} + A_{yt} \rangle &= 0, \quad \langle uA_{xt} + vA_{yt} + A_{tt} \rangle = 0. \end{aligned} \quad (16)$$

After the determination of the distribution function $f(x, y, t, u, v, \xi)$, the flux along the interface $x = x_{i+1/2}, y \in [y_{j-1/2}, y_{j+1/2}]$ is

$$\begin{aligned} F(y, t) &= \int u f \psi d\Xi = F^c(y, t) - F^v(y, t), \\ F^v(y, t) &= \tau \int u D g \psi d\Xi \\ &= \tau [\langle u^2 a_x + u v a_y + u a_t \rangle + \langle u^2 A_{xx} + u v A_{xy} + u A_{yt} \rangle y + \langle u^2 A_{xt} + u v A_{yt} + u A_{tt} \rangle t], \\ F^c(y, t) &= [\rho U, \rho U^2 + p, \rho UV, (E + p)U]^T, \end{aligned} \quad (17)$$

where (ρ, U, V, E, p) are determined by $W(y, t)$, which is the conservative variables corresponding to g ,

$$W(y, t) = \int g \psi d\Xi = W^e + \langle a_y \rangle y + \langle a_t \rangle t + \frac{1}{2} (\langle A_{yy} \rangle y^2 + \langle A_{tt} \rangle t^2) + \langle A_{yt} \rangle yt, \quad (18)$$

and W^e is determined by g^e .

It is well known that the above space and time evolving gas distribution function corresponds to a flow with unit Prandtl number. To correct the Prandtl number, we can change the heat-flux

$$q = \frac{1}{2} \int (u - U)[(u - U)^2 + (v - V)^2 + \xi^2] f d\Xi = U F_2^v + V F_3^v - F_4^v, \quad (19)$$

where velocity U and V are defined by

$$U = \int u f d\Xi / \int f d\Xi, \quad V = \int v f d\Xi / \int f d\Xi. \quad (20)$$

The above heat flux can be used to modify the energy transport to get any Prandtl number needed,

$$F_4^{Fix} = F_4 + (1/Pr - 1)q. \quad (21)$$

To compute the final numerical flux transport along the cell interface within a time step,

$$\hat{F}_{i+1/2, j} = \int_{t^n}^{t^{n+1}} \int_{y_{j-1/2}}^{y_{j+1/2}} F(y, t) dy dt, \quad (22)$$

we can set two Gaussian points y_{G1} and y_{G2} at the interface $x = x_{i+1/2}, y \in [y_{i-1/2}, y_{i+1/2}]$, and two Gaussian points t_{G1} and t_{G2} in time between $t \in [t^n, t^{n+1}]$. At these points, the flow variables U and V can be obtained from $g(x, y, t, u, v, \xi)$, and F by (17), where the aforementioned Prandtl fix is used to obtain the modified F_4^{Fix} . Then, we can use this modified flux F^{Fix} to compute the numerical flux (22) by Gaussian quadrature

$$\hat{F}_{i+1/2,j} = \frac{\Delta t \Delta y}{4} [F^{Fix}(y_{G1}, t_{G1}) + F^{Fix}(y_{G1}, t_{G2}) + F^{Fix}(y_{G2}, t_{G1}) + F^{Fix}(y_{G2}, t_{G2})]. \quad (23)$$

The same procedures can be applied to obtain the numerical flux along y -direction interface $y = y_{j+1/2}, x \in [x_{i-1/2}, x_{i+1/2}]$, which is denoted by $\hat{G}_{i,j+1/2}$.

After these procedures the local conservative law is used to update the cell averaged conservative variables

$$\begin{aligned} \bar{W}_{ij}^{n+1} &= \bar{W}_{ij}^n + \frac{1}{\Delta x \Delta y} \int_{t_n}^{t_{n+1}} \int_{y_{j-1/2}}^{y_{j+1/2}} [F(t, x_{i-1/2}, y) - F(t, x_{i+1/2}, y)] dy dt \\ &+ \frac{1}{\Delta x \Delta y} \int_{t_n}^{t_{n+1}} \int_{x_{i-1/2}}^{x_{i+1/2}} [G(t, x, y_{j-1/2}) - G(t, x, y_{j+1/2})] dx dt \\ &= \bar{W}_{i,j}^n - \frac{(\hat{F}_{i+1/2,j} - \hat{F}_{i-1/2,j}) + (\hat{G}_{i,j+1/2} - \hat{G}_{i,j-1/2})}{\Delta x \Delta y}. \end{aligned} \quad (24)$$

Remarks:

(a). Here we use the Gaussian quadrature (not analytic integration) to compute the integration in time and space. In one-dimensional case, this approach can make the scheme be more stable. In two-dimensional case, this approach can keep the time accuracy of the scheme. For both one and two dimensional cases, this approach can save computational time.

(b). Based on the 5th-order WENO interpolation, we will use characteristic variables to calculate the values and spatial derivatives of conservative variables at cell interfaces. The scheme presented above has a 3rd-order accuracy in time. As to the spatial accuracy, in one-dimensional case the current scheme can reach a 5th-order accuracy. While for two-dimensional cases, the integration of fluxes along the cell interface is based on a 2nd-order polynomial, and the 3rd-order term (y^3) disappears in the integration. So, the Gaussian quadrature used in this scheme has a 4th-order in error, and the scheme is 4th-order accurate. We will numerically validate the order of the scheme.

3. The 5th-order WENO reconstruction

In this paper we use Yamaleev and Carpenter's new WENO weight [28], which has high resolution in capturing discontinuities and fast convergence of the 5th-order WENO to the corresponding underlying linear scheme. To enhance the performance, a slight modification on the weights has been proposed in the following.

3.1. One-dimensional 5th-order WENO interpolation

Following standard approaches, we will use the characteristic variables for the interpolation of the cell interface values.

1. With the cell averaged conservative variables \bar{W}_i , at the cell interface $i + 1/2$, the averaged value is $\bar{W}_{i+1/2} = (\bar{W}_i + \bar{W}_{i+1})/2$, which is used to calculate the left and right eigenvector matrix $L_{i+1/2}$ and $R_{i+1/2}$ and the characteristic value (eigenvalues) $c_\alpha (\alpha = 1, 2, 3)$.

2. Change the conservative variables $\bar{W}_{i+l} (l = -2, \dots, 3)$ to characteristic ones \tilde{W}_{i+l} by

$$\tilde{W}_{i+l} = L_{i+1/2} \bar{W}_{i+l}. \quad (25)$$

3. For α -th component, consider the following interpolation,

$$\begin{aligned} W_{\alpha,i+1/2}^1 &= \frac{11}{6} \tilde{W}_{\alpha,i} - \frac{7}{6} \tilde{W}_{\alpha,i-1} + \frac{1}{3} \tilde{W}_{\alpha,i-2}, & W_{\alpha,i+1/2}^2 &= \frac{5}{6} \tilde{W}_{\alpha,i} + \frac{1}{3} \tilde{W}_{\alpha,i+1} - \frac{1}{6} \tilde{W}_{\alpha,i-1}, \\ W_{\alpha,i+1/2}^3 &= \frac{5}{6} \tilde{W}_{\alpha,i+1} - \frac{1}{6} \tilde{W}_{\alpha,i+2} + \frac{1}{3} \tilde{W}_{\alpha,i}, & W_{\alpha,i+1/2}^4 &= \frac{11}{6} \tilde{W}_{\alpha,i+1} - \frac{7}{6} \tilde{W}_{\alpha,i+2} + \frac{1}{3} \tilde{W}_{\alpha,i+3}, \\ IS_1 &= \frac{13}{12} (\tilde{W}_{i-2} - 2\tilde{W}_{i-1} + \tilde{W}_i)^2 + (\tilde{W}_{i-2} - 3\tilde{W}_{i-1} + 2\tilde{W}_i)^2, \\ IS_2 &= \frac{13}{12} (\tilde{W}_{i-1} - 2\tilde{W}_i + \tilde{W}_{i+1})^2 + (\tilde{W}_i - \tilde{W}_{i+1})^2, \\ IS_3 &= \frac{13}{12} (\tilde{W}_i - 2\tilde{W}_{i+1} + \tilde{W}_{i+2})^2 + (\tilde{W}_i - \tilde{W}_{i+1})^2, \\ IS_4 &= \frac{13}{12} (\tilde{W}_{i+3} - 2\tilde{W}_{i+2} + \tilde{W}_{i+1})^2 + (\tilde{W}_{i+3} - 3\tilde{W}_{i+2} + 2\tilde{W}_{i+1})^2, \\ \beta_{1s} &= d_{1s} [1 + \sigma_1^2 / (IS_s^2 + \epsilon)] (s = 1, 2, 3), & d_{11} &= 1/10, \quad d_{12} = 3/5, \quad d_{13} = 3/10, \quad \epsilon = 1e - 6; \\ \sigma_1 &= \tilde{W}_{i-2} - 4\tilde{W}_{i-1} + 6\tilde{W}_i - 4\tilde{W}_{i+1} + \tilde{W}_{i+2} \\ w_{1s} &= \beta_{1s} / \sum_{p=1}^3 \beta_{1p} (s = 1, 2, 3), & \tilde{W}_{\alpha,i+1/2}^- &= \sum_{s=1}^3 w_{1s} W_{\alpha,i+1/2}^s; \\ \beta_{2s} &= d_{2s} [1 + \sigma_2^2 / (IS_{s+1}^2 + \epsilon)] (s = 1, 2, 3), & d_{21} &= 3/10, \quad d_{22} = 3/5, \quad d_{23} = 1/10; \\ \sigma_2 &= \tilde{W}_{i+3} - 4\tilde{W}_{i+2} + 6\tilde{W}_{i+1} - 4\tilde{W}_i + \tilde{W}_{i-1} \\ w_{2s} &= \beta_{2s} / \sum_{p=1}^3 \beta_{2p} (s = 1, 2, 3), & \tilde{W}_{\alpha,i+1/2}^+ &= \sum_{s=1}^3 w_{2s} W_{\alpha,i+1/2}^{s+1}. \end{aligned} \quad (26)$$

It should be noted that Yamaleev and Carpenter [28] used

$$\beta_s = d_s (1 + \sigma_1^2 / (IS_s + \epsilon)). \quad (27)$$

Instead, we use

$$\beta_s = d_s (1 + \sigma_1^2 / (IS_s^2 + \epsilon)). \quad (28)$$

Our numerical experiments show that (27) will generate small oscillations which can be effectively suppressed by using (28).

Set $\epsilon_0 = 1e - 3$, if $c_\alpha > \epsilon_0$, we only interpolate $\tilde{W}_{\alpha,i+1/2}^-$ and calculate $W_{i+1/2} = R_{i+1/2}\tilde{W}_{i+1/2}^-$. If $c < -\epsilon_0$, we just interpolate $\tilde{W}_{\alpha,i+1/2}^+$ to calculate $W_{i+1/2} = R_{i+1/2}\tilde{W}_{i+1/2}^+$. But, if $-\epsilon_0 \leq c_\alpha \leq \epsilon_0$, we will make the following computation.

$$\beta_1 = \sqrt{c_\alpha^2 + \epsilon} + c_\alpha, \quad \beta_2 = \sqrt{c_\alpha^2 + \epsilon} - c_\alpha, \quad w_s = \beta_s / \sum_{p=1}^2 \beta_p (s = 1, 2), \quad (29)$$

$$\tilde{W}_{\alpha,i+1/2} = w_1 \tilde{W}_{\alpha,i+1/2}^- + w_2 \tilde{W}_{\alpha,i+1/2}^+, \quad W_{i+1/2} = R_{i+1/2} \tilde{W}_{i+1/2}.$$

These manipulation can save computational cost, because for most cases and great parts of flow field, c_α is not belong to $[-\epsilon_0, \epsilon_0]$. Hence only $\tilde{W}_{i+1/2}^-$ or $\tilde{W}_{i+1/2}^+$ (not both of them) should be calculated.

The derivatives at the cell interface are interpolated as

$$\left. \frac{\partial W_\alpha}{\partial x} \right|_{i+1/2} = \frac{1.25(\bar{W}_{\alpha,i+1} - \bar{W}_{\alpha,i}) + \bar{W}_{\alpha,i-1} - \bar{W}_{\alpha,i+2}}{\Delta x}, \quad (30)$$

$$\left. \frac{\partial^2 W_\alpha}{\partial x^2} \right|_{i+1/2} = \frac{31(\bar{W}_{\alpha,i} + \bar{W}_{\alpha,i+1}) - \bar{W}_{\alpha,i-1} - \bar{W}_{\alpha,i+2} - 60W_{\alpha,i+1/2}}{8\Delta x^2}.$$

Numerical tests confirm that it is not necessary to use WENO interpolation in calculating the derivatives. Similar phenomenon has been observed previously by J. Qiu [17].

3.2. Two-dimensional 5th-order WENO interpolation

In two-dimensional cases, the cell averaged values are

$$\bar{W}_{i,j} = \int_{y_{j-1/2}}^{y_{j+1/2}} \int_{x_{i-1/2}}^{x_{i+1/2}} W dx dy. \quad (31)$$

So if we adopt the above one-dimensional 5th-order WENO interpolation, such as in the x -direction, we will obtain the line averaged W and its derivatives along the cell interface,

$$W_{i+1/2,j}^y = \frac{1}{\Delta y} \int_{y_{j-1/2}}^{y_{j+1/2}} W dy, \quad W_{x,i+1/2,j}^y = \frac{1}{\Delta y} \int_{y_{j-1/2}}^{y_{j+1/2}} \partial_x W dy, \quad (32)$$

$$W_{xx,i+1/2,j}^y = \frac{1}{\Delta y} \int_{y_{j-1/2}}^{y_{j+1/2}} \partial_{xx} W dy.$$

In the y -direction, similar procedures lead to $W_{i,j+1/2}^x$, $W_{y,i,j+1/2}^x$, and $W_{yy,i,j+1/2}^x$. To extract the values and derivatives of the conservative variables around the center point of a cell interface $x = x_{i+1/2}$, $y \in [y_{j-1/2}, y_{j+1/2}]$, we will use the line averaged $W_{i+1/2,j-2}^y$, $W_{i+1/2,j-1}^y$, $W_{i+1/2,j}^y$, $W_{i+1/2,j+1}^y$,

and $W_{i+1/2,j+2}^y$ to reconstruct $W_{i+1/2,j}$ up to 3rd-order accuracy. In detail, the reconstructed central values are

$$\begin{aligned} W^1 &= \frac{23W_{i+1/2,j}^y - W_{i+1/2,j-2}^y + 2W_{i+1/2,j-1}^y}{24}, \\ W^2 &= \frac{26W_{i+1/2,j}^y - W_{i+1/2,j-1}^y - W_{i+1/2,j+1}^y}{24}, \\ W^3 &= \frac{23W_{i+1/2,j}^y - W_{i+1/2,j+2}^y + 2W_{i+1/2,j+1}^y}{24}, \end{aligned} \quad (33)$$

$$\begin{aligned} IS_1 &= \frac{13}{3}(W_{i+1/2,j}^y + W_{i+1/2,j-2}^y - 2W_{i+1/2,j-1}^y)^2 + (3W_{i+1/2,j}^y + W_{i+1/2,j-2}^y - 4W_{i+1/2,j-1}^y)^2, \\ IS_2 &= \frac{13}{3}(W_{i+1/2,j+1}^y + W_{i+1/2,j-1}^y - 2W_{i+1/2,j}^y)^2 + (W_{i+1/2,j+1}^y - W_{i+1/2,j-1}^y)^2, \\ IS_3 &= \frac{13}{3}(W_{i+1/2,j+2}^y + W_{i+1/2,j}^y - 2W_{i+1/2,j+1}^y)^2 + (3W_{i+1/2,j}^y + W_{i+1/2,j+2}^y - 4W_{i+1/2,j+1}^y)^2, \end{aligned} \quad (34)$$

$$\begin{aligned} \beta_s &= 1 + \sigma^2 / (IS_s^2 + \epsilon) \quad (s = 1, 2, 3), \quad \epsilon = 1e - 6; \\ \sigma &= W_{i+1/2,j-2}^y - 4(W_{i+1/2,j-1}^y + W_{i+1/2,j+1}^y) + 6W_{i+1/2,j}^y + W_{i+1/2,j+2}^y, \\ w_s &= \beta_s / \sum_{p=1}^3 \beta_p \quad (s = 1, 2, 3), \quad W_{i+1/2,j} = \sum_{s=1}^3 w_s W^s. \end{aligned} \quad (35)$$

Then, we use center stencil $[j - 1, j, j + 1]$ to interpolate their derivatives

$$\begin{aligned} \partial_y W_{i+1/2,j} &= \frac{W_{i+1/2,j+1}^y - W_{i+1/2,j-1}^y}{2\Delta y}, \\ \partial_{yy} W_{i+1/2,j} &= \frac{W_{i+1/2,j-1}^y + W_{i+1/2,j+1}^y - 2W_{i+1/2,j}^y}{\Delta y^2}, \\ \partial_x W_{i+1/2,j} &= \frac{26W_{x,i+1/2,j}^y - W_{x,i+1/2,j-1}^y - W_{x,i+1/2,j+1}^y}{24}, \\ \partial_{xy} W_{i+1/2,j} &= \frac{W_{x,i+1/2,j+1}^y - W_{x,i+1/2,j-1}^y}{2\Delta y}, \\ \partial_{xx} W_{i+1/2,j} &= \frac{26W_{xx,i+1/2,j}^y - W_{xx,i+1/2,j-1}^y - W_{xx,i+1/2,j+1}^y}{24}. \end{aligned} \quad (36)$$

Our numerical experiments show that these simple center interpolations work very well in both smooth and discontinuous regions.

4. Monotonicity-preserving limiter

Different from previous GKS scheme [24], which uses discontinuous initial reconstruction, in the current scheme a continuous initial reconstruction with WENO interpolation is adopted. The numerical experiments show that for weak shock, the current WENO-GKS is sufficient enough to suppress the numerical oscillation. But when the shock is strong, there still appears oscillation near the discontinuity, which sometimes even causes blowup. So we will add monotonicity-preserving limiter (MP-limiter) to suppress the oscillations. The MP-limiter was firstly invented by Suresh and Huynh [20], which was used to constrain the interpolation of characteristic variables. Later, Daru and Tenaud [5] created a MP-limiter based on point flux values, which was further modified to a more sophisticated version [6]. The MP-limiter can preserve monotonicity in solving the linear equation without losing accuracy in smooth region, except for the point where the first three derivatives disappear [1]. At this time, the scheme will not surpass 4th-order accuracy. For nonlinear equations, the MP-limiter can also effectively suppress the numerical oscillation near discontinuity. The scheme with the combination of the above WENO-GKS and the MP-limiter is named MPWENO-GKS. The combination of the WENO and the MP-limiter has been used early. In 2000, Balsara and Shu [1] had already successfully added the MP-limiter to the classical WENO scheme to improve the performances of high order WENO. In the current MPWENO-GKS, we will implement Daru and Tenaud's flux-value based MP-limiter [6].

5. Numerical Experiments

5.1. Stability Test

In the following paragraphs, to emphasize the reconstruction order, we will call current schemes MPWENO5-GKS (with MP-limiter) and WENO5-GKS (without MP-limiter). The MPWENO5-GKS is a highly nonlinear scheme. We explore the stability property numerically using a test case for the Euler equations with initial conditions

$$\rho = 1 + \frac{1}{4} \sin\left(\frac{2\pi}{5}\right), \quad U = 1, \quad p = 1, \quad (37)$$

where ρ is density, U is velocity, and p is pressure. Periodic boundary conditions are set at both ends in the computational domain $x \in [-5, 5]$. The numerical experiments show that the maximum stable CFL number can reach 1.05.

5.2. Accuracy test

To get the accuracy of the schemes, we use the same flow condition (37) to test the inviscid solutions. The original Jiang and Shu's WENO scheme [8] is named WENO5-JS. The WENO5-JS with the modification of Yamaleev and Carpenter's weight [8, 28] is named WENO5-JS-1. Yamaleev and Carpenter [28] had already verified that the errors of WENO5-JS-1 is smaller than WENO5-JS.

Table 1: The errors of 5th-order WENO-JS-1.

N	20	40	80	160	320
L_1 error	6.473e-3	2.250e-4	6.965e-6	2.183e-7	6.819e-9
Order	–	4.85	5.01	5.00	5.00
L_∞ error	1.087e-2	4.094e-4	2.230e-5	3.700e-7	1.156e-8
Order	–	4.73	4.20	5.91	5.00

Table 2: The errors of WENO5-GKS.

N	20	40	80	160	320
L_1 error	3.144e-3	1.073e-4	3.170e-6	9.943e-8	3.111e-9
Order	–	4.87	5.08	4.99	5.00
L_∞ error	6.422e-3	2.530e-4	5.350e-6	1.563e-7	4.887e-9
Order	–	4.66	5.56	5.10	5.00

Table 3: The errors of MPWENO5-GKS.

N	20	40	80	160	320
L_1 error	3.141e-3	1.070e-4	3.171e-6	9.946e-8	3.112e-9
Order	–	4.88	5.08	4.99	5.00
L_∞ error	6.430e-3	2.504e-4	5.329e-6	1.599e-7	5.765e-9
Order	–	4.68	5.55	5.06	4.79

Table 4: The time errors of WENO5-GKS.

Δt	1.189e-2(.9)	1.057e-2(.8)	9.245e-3(.7)	7.924e-3(.6)	6.603e-3(.5)
L_1 error	2.797e-7	1.972e-7	1.331e-7	8.487e-8	5.032e-8
Order	–	2.97	2.95	2.92	2.87
L_∞ error	4.394e-7	3.098e-7	2.090e-7	1.333e-7	7.903e-8
Order	–	2.97	2.95	2.92	2.87

Table 5: The time errors of MPWENO5-GKS.

Δt	1.453e-2(1.1)	1.321e-2(1.0)	1.189e-2(.9)	1.057e-2(.8)	9.245e-3(.7)	7.924e-3(.6)
L_1 error	5.323e-7	4.153e-7	3.178e-7	2.391e-7	1.764e-7	1.276e-7
Order	–	2.60	2.54	2.42	2.28	2.10
L_∞ error	2.398e-6	2.141e-6	1.892e-6	1.650e-6	1.416e-6	1.190e-6
Order	–	1.19	1.17	1.16	1.14	1.13

So we just compare the errors of current schemes with WENO5-JS-1. The errors of the WENO5-JS-1, WENO5-GKS, and MPWENO5-GKS are shown in Table 1, Table 2, and Table 3 respectively. In all of these tables N is grid number.

The above tables show that all three schemes have the 5th-order accuracy, while the WENO5-GKS and MPWENO5-GKS have smaller errors in magnitude than that of the WENO5-JS-1, and the errors of the MPWENO5-GKS are almost the same as those of the WENO5-GKS, which means that the implementation of the MP-limiter does not deteriorate the scheme's accuracy in this test case.

The time accuracy of the WENO-GKS and MPWENO-GKS is also tested. Table 4 and Table 5 show the errors of the WENO5-GKS and MPWENO5-GKS on a fixed grid number $N = 320$ but with different time steps. The numbers in the parenthesis in the time step row are the corresponding CFL numbers. Hence the WENO5-GKS is of 3rd-order accurate in time while the MPWENO5-GKS has only about 2nd-order accuracy when time step is small. Only when time step is large, the MPWENO5-GKS approaches to its designed 3rd-order accuracy. But, the MPWENO5-GKS is more stable than the WENO5-GKS. Our experiments show that there appears negative pressure when we set $CFL = 1.0$ for the WENO5-GKS. When comparing the magnitude of the errors, we can see that the absolute errors of the MPWENO5-GKS are close to those of the WENO5-GKS. Therefore deterioration of time accuracy is acceptable.

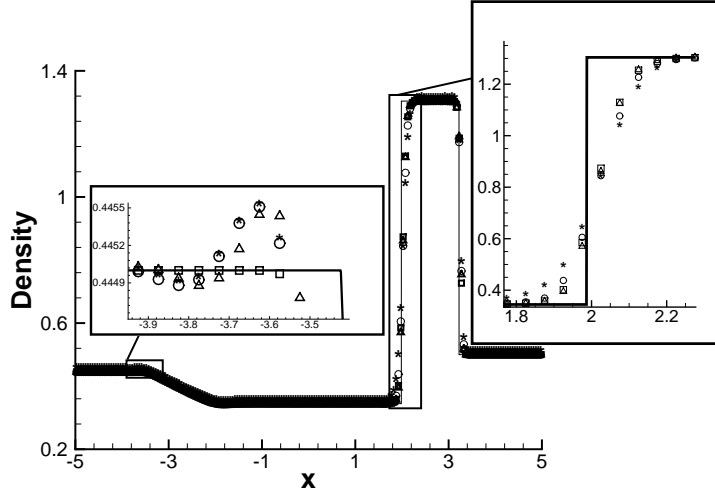


Figure 1: Lax problem by different schemes on grid $N = 200$. Density profiles. Solid line: exact solution; square: MPWENO5-GKS; delta: WENO5-GKS; circle: WENO5-JS-1; asterisk: WENO5-JS. The boxed regions are zoomed in.

5.3. Discontinuous flow tests and computational efficiency

For flows with discontinuous structures, we compare the results from the MPWENO5-GKS, the WENO5-GKS, WENO5-JS, and the WENO5-JS-1. In the following test cases, the CFL number is set to be 0.5.

Example 4.1 Lax problem

Solve the Euler equations with the Riemann initial condition:

$$\begin{aligned} (\rho, U, p) &= (0.445, 0.698, 3.528) \quad \text{for } x \in [-5, 0], \\ (\rho, U, p) &= (0.5, 0, 0.571) \quad \text{for } x \in (0, 5]. \end{aligned} \quad (38)$$

The computational domain is covered with $N = 200$ grid points, and the output time is $t = 1.3$. Fig. 1 shows that all four schemes obtain acceptable results. In the zoomed blocks we can see that MPWENO5-GKS and WENO5-GKS have higher resolution in capturing discontinuity than the rest two schemes. Especially the MPWENO5 does not present oscillations at the corner of rarefaction wave. Velocity and pressure by the MPWENO5-GKS are shown in Fig. 2.

Example 4.2 Blast wave problem

The Woodward-Colella blast wave problem [22] is computed in domain $x \in [-5, 5]$ with initial

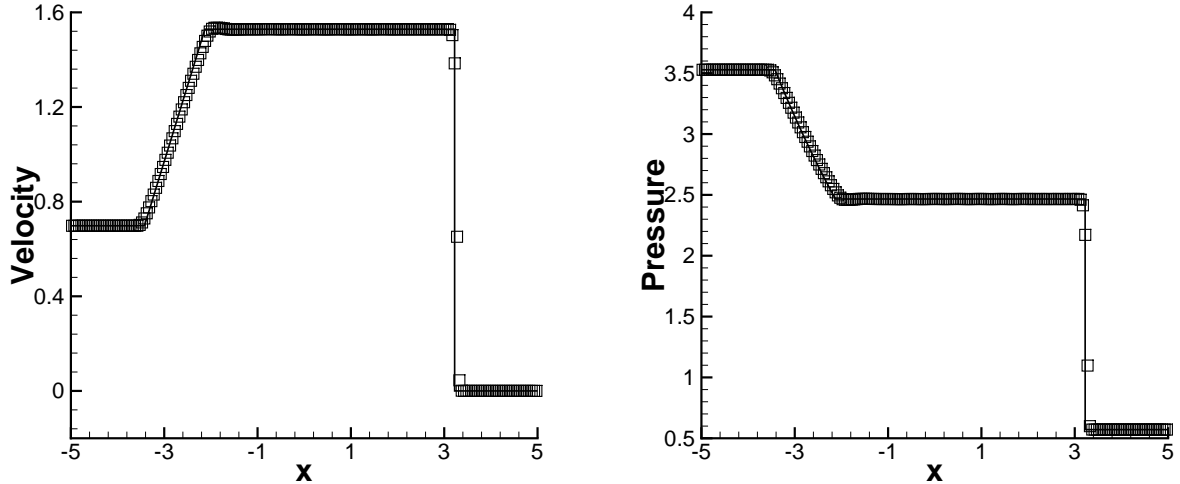


Figure 2: Lax problem by MPWENO5-GKS on grid $N = 200$. Left: velocity, right: pressure.

condition

$$\rho = 1; \quad U = 0; \quad p = \begin{cases} 1000, & x \in [0, -4), \\ 0.01, & x \in [-4, 4), \\ 100, & x \in [4, 5]. \end{cases} \quad (39)$$

The output time is $t = 0.38$. The density profiles on grids $N = 200$ and $N = 400$ by the MPWENO5-GKS and WENO5-JS are compared in figure 3. For this case the WENO5-GKS and the WENO5-JS-1 failed. The reference solution is obtained by WENO5-JS on $N = 10000$ grids. We can see that the MPWENO5-GKS has better resolution in comparison with WENO5-JS.

Example 4.3 Shock acoustic-wave interaction

The Shu-Osher shock acoustic-wave interaction problem [18] is computed in a domain $x \in [-5, 5]$ with initial condition

$$(p, U, \rho) = \begin{cases} (3.857134, 2.629369, 10.33333), & x < -4, \\ (1 + 0.2 \sin(5x), 0, 1), & x \geq -4. \end{cases} \quad (40)$$

The computation time is $t = 1.8$. The reference solution is obtained by WENO5-JS with $N = 5000$ grid points. Figure 4 shows that both the MPWENO5-GKS and WENO5-GKS have better resolution for short waves than WENO5-JS and WENO5-JS-1, while the MPWENO5-GKS and WENO5-GKS have similar performance.

We use the above examples 4.1-4.3 to test the computational efficiency of the current MPWENO5-GKS and WENO5-GKS schemes. In the experiments the grid number is $N = 200$ and the time step

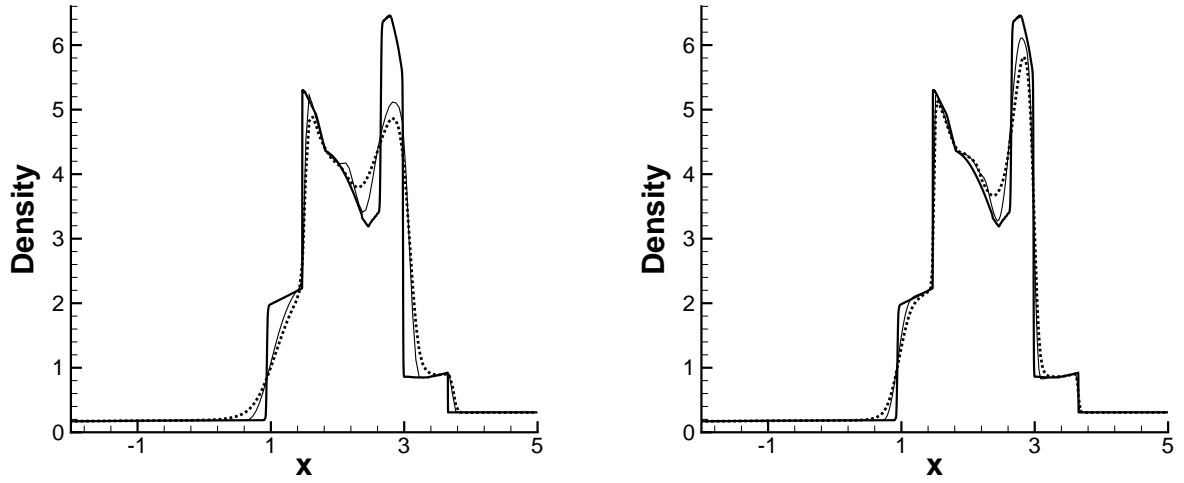


Figure 3: Blasting wave problem. Density profiles. Thick solid: reference solution (WENO5-JS with $N = 10000$); thin solid: MPWENO5-GKS; dotted: WENO5-JS. Left: $N = 200$; right $N = 400$.

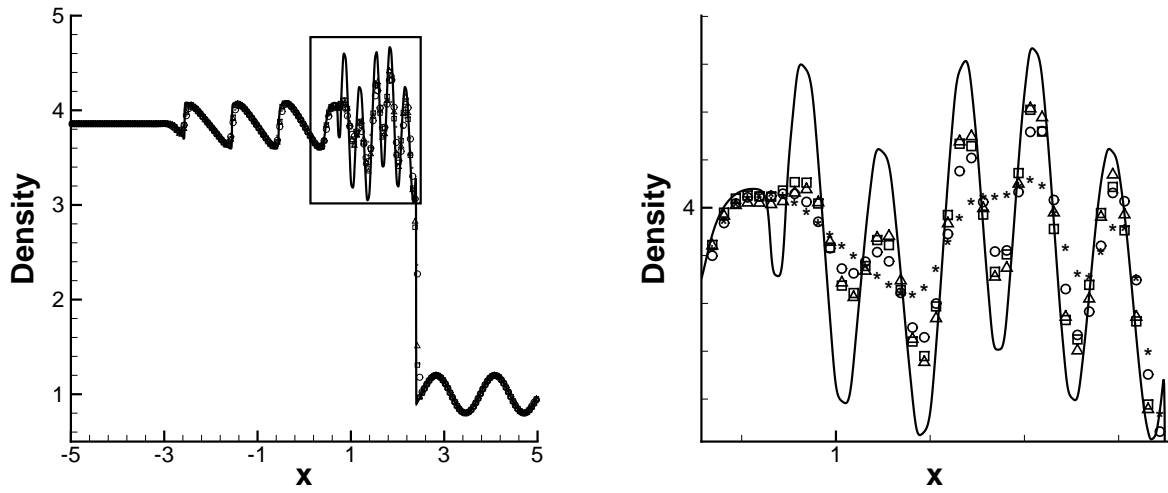


Figure 4: Shu-Osher problem on grid $N = 200$. Density profiles. The right: zoomed-in plot of the boxed region in left figure. Solid line: reference solution; square: MPWENO5-GKS; delta: WENO5-GKS; circle: WENO5-JS-1; asterisk: WENO5-JS.

Table 6: CPU times for different schemes and test cases.

	Lax Problem	Shu-Osher	Blast wave
WENO5-GKS	0.187s	0.281s	–
MPWENO5-GKS	0.234s	0.328s	0.624s
WENO5-JS	0.343s	0.483s	0.905s
WENO5-JS-1	0.359s	0.499s	–

is determined by $CFL = 0.5$. The CPU time costs are shown in Table 6. From this comparison, we can observe that the WENO5-GKS is the most efficient method among all four schemes, and the finite volume MPWENO5-GKS is still about 0.5 times faster than the finite difference WENO5-JS.

5.4. Two dimensional cases

Now we validate the MPWENO5-GKS and WENO5-GKS in two-dimensional space.

5.4.1. Accuracy test

Example 4.4 Convection of isotropic vortex for two-dimensional Euler equations

The periodic vortex problem is set up in a computational domain $[0, 10] \times [0, 10]$. The boundary condition is periodic in both directions. The initial conditions are given by

$$\begin{aligned} (w_1(x, y, 0), w_2(x, y, 0)) &= (1, 1) + \frac{\epsilon}{2\pi} e^{0.5(1-r^2)}(-\bar{y}, \bar{x}), \\ T(x, y, 0) &= 1 - \frac{(\gamma - 1)\epsilon^2}{8\gamma\pi^2} e^{1-r^2}, \quad S(x, y, 0) = 1, \end{aligned} \quad (41)$$

where the temperature T and the entropy S are related to the density ρ and the pressure p by

$$T = p/\rho, S = p/\rho^\gamma, \quad (42)$$

$(\bar{x}, \bar{y}) = (x - 5, y - 5)$, $r^2 = \bar{x}^2 + \bar{y}^2$, $\gamma = 1.4$, and the vortex strength $\epsilon = 5$. The exact solution is an isotropic vortex convected with the speed $(U, V) = (1, 1)$ in the diagonal direction. The numerical experiment shows that for isotropic vortex convection the stable condition is $CFL \leq 0.875$ for the WENO5-GKS and $CFL \leq 0.704$ for the MPWENO5-GKS.

To test the accuracy, we make the calculation up to $t = 10$, namely one time period. The L_1 and L_∞ errors of the WENO5-GKS and the MPWENO5-GKS are shown in Table 7. The WENO5-GKS has reached its designed 4th-order, but the MPWENO5-GKS is only 3rd-order for this problem. The reason is that for this problem the MPWENO5-GKS loses the accuracy at the points connecting the horizontal and the curved part in the velocity profile. This property of the

Table 7: Euler equation; convection of isotropic vortex; periodic boundary conditions. Compare the errors of WENO5-GKS and MPWENO5-GKS.

N	WENO5-GKS				MPWENO5-GKS			
	L_1 error	Order	L_∞ error	Order	L_1 error	Order	L_∞ error	Order
31	1.083e-3	–	2.378e-2	–	1.339e-3	–	2.422e-2	–
36	6.302e-4	3.62	1.323e-2	3.92	8.192e-4	3.29	1.400e-2	3.67
41	3.731e-4	4.03	7.491e-3	4.37	5.138e-4	3.59	8.456e-3	3.88
46	2.221e-4	4.51	4.429e-3	4.57	3.500e-4	3.34	5.127e-3	4.35
51	1.386e-4	4.57	2.687e-3	4.84	2.530e-4	3.15	4.563e-3	1.13

Table 8: Euler equation; convection of density sine wave; periodic boundary conditions. Compare the errors of WENO5-GKS and MPWENO5-GKS.

N	WENO5-GKS				MPWENO5-GKS			
	L_1 error	Order	L_∞ error	Order	L_1 error	Order	L_∞ error	Order
31	1.796e-3	–	3.926e-3	–	1.795e-3	–	4.861e-3	–
36	9.504e-4	4.26	1.994e-3	4.53	9.517e-4	4.24	1.947e-3	6.12
41	5.477e-4	4.24	1.149e-3	4.24	5.507e-4	4.21	1.106e-3	4.35
46	3.387e-4	4.18	6.875e-4	4.46	3.400e-4	4.19	6.724e-4	4.32
51	2.207e-4	4.15	4.403e-4	4.32	2.214e-4	4.16	4.320e-4	4.29

MP-limiter has already been pointed out by Suresh and Huynh [20], and Balsara and Shu [1]. We further validate the order of WENO5-GKS and MPWENO5-GKS with Euler equation under the initial condition

$$(\rho, U, V, p) = (1 + \sin(\frac{2\pi x}{5}) \sin(\frac{2\pi y}{5}), 1, 1, 1), \quad (43)$$

and periodic boundary condition at both directions of computational domain $[0, 10] \times [0, 10]$. The one-period $t = 10$ errors are show in Table 8, where both WENO5-GKS and MPWENO-GKS reach the designed 4th-order.

The efficiency of WENO5-GKS, MPWENO5-GKS and WENO5-JS (finite difference 5th-order WENO with local Lax-Friedrich flux splitting) is tested in this case as well. To compute the isotropic vortex convection problem with a mesh 101×101 , $CFL = 0.1$, and the output time $t = 10$, the CPU costs of different schemes are shown in Table 9. This comparison shows that MPWENO5-GKS is slightly faster than WENO5-JS, and WENO5-GKS is more efficient than MPWENO5-GKS. For the NS equations, in the current GKS, the viscous term can be simply added to the flux by (17), which costs much less CPU time than the interpolation of viscous terms in WENO-JS. Therefore,

Table 9: CPU times for different schemes and test cases.

	WENO5-GKS	MPWENO5-GKS	WENO5-JS
CPU cost	71.18s	98.05s	101.37s

for NS simulation, MPWENO5-GKS will become more efficient than WENO-JS.

Example 4.5 Shock-Vortex interaction

We compute the shock-vortex interaction problem [3]. In the computational domain $(x, y) \in [0, 2] \times [0, 1]$, a stationary shock front is positioned at $x = 0.5$. The left upstream state is $(\rho, U, V, p) = (M^2, \sqrt{\gamma}, 0, 1)$, where γ is the specific heat ratio and M is the Mach number. A small vortex is a perturbation on the mean flow with the velocity (U, V) , temperature $(T = p/\rho)$ and entropy $(S = \ln(\frac{p}{\rho^\gamma}))$, where the perturbation is

$$\tilde{U} = \kappa\eta e^{\mu(1-\eta^2)} \sin \theta, \quad \tilde{V} = -\kappa\eta e^{\mu(1-\eta^2)} \cos \theta, \quad \tilde{T} = -\frac{(\gamma - 1)\kappa^2 e^{2\mu(1-\eta^2)}}{4\mu\gamma}, \quad \tilde{S} = 0, \quad (44)$$

where $\eta = r/r_c$, $r = \sqrt{(x - x_c)^2 + (y - y_c)^2}$, $(x_c, y_c) = (0.25, 0.5)$ is the center of the vortex, η and μ control the strength and decay rate of the vortex, and r_c is the critical radius. Here we choose $\kappa = 0.3$, $r_c = 0.05$ and $\alpha = 0.204$.

The gas is set to be a diatomic molecule with $\gamma = 1.4$ and $CFL = 0.5$. The grid number is 202×101 . The reflecting boundary condition is used on the top and bottom boundaries. The evolution of the flow is given in figure 5 ($CFL = 0.1$). In this case, the WENO5-GKS gives better results, see figure 6 ($CFL = 0.5$). The experiments show that for the MPWENO5-GKS a large CFL number gives oscillatory results. A reference solution by WENO5-JS on a grid 1202×601 is shown in figure 7

Example 4.6 Double Mach reflection problem.

The computation domain is $[0, 4] \times [0, 1]$. A solid wall lies at the bottom of the computational domain starting from $x = 1/6$. Initially a right-moving Mach 10 shock is positioned at $x = 1/6, y = 0$ and makes a 60° angle with the x -axis. For the bottom boundary, the exact post-shock condition is imposed for the part from $x = 0$ to $x = 1/6$ and an Euler reflecting boundary condition is used for the rest. At the top boundary of the computational domain, the flow values are set to describe the exact motion of the Mach 10 shock. The initial pre-shock condition is

$$(\rho, p, u, v) = (8, 116.5, 8.25 \cos(30^\circ), -8.25 \sin(30^\circ)), \quad (45)$$

and the post-shock condition is

$$(\rho, p, u, v) = (1.4, 1, 0, 0). \quad (46)$$

We compute the solution up to $t = 0.2$. Uniform meshes with 960×240 cells are used. In figure 8 we show 30 equally spaced density contours from 1.5 to 22.7. The zoomed profile around tripe

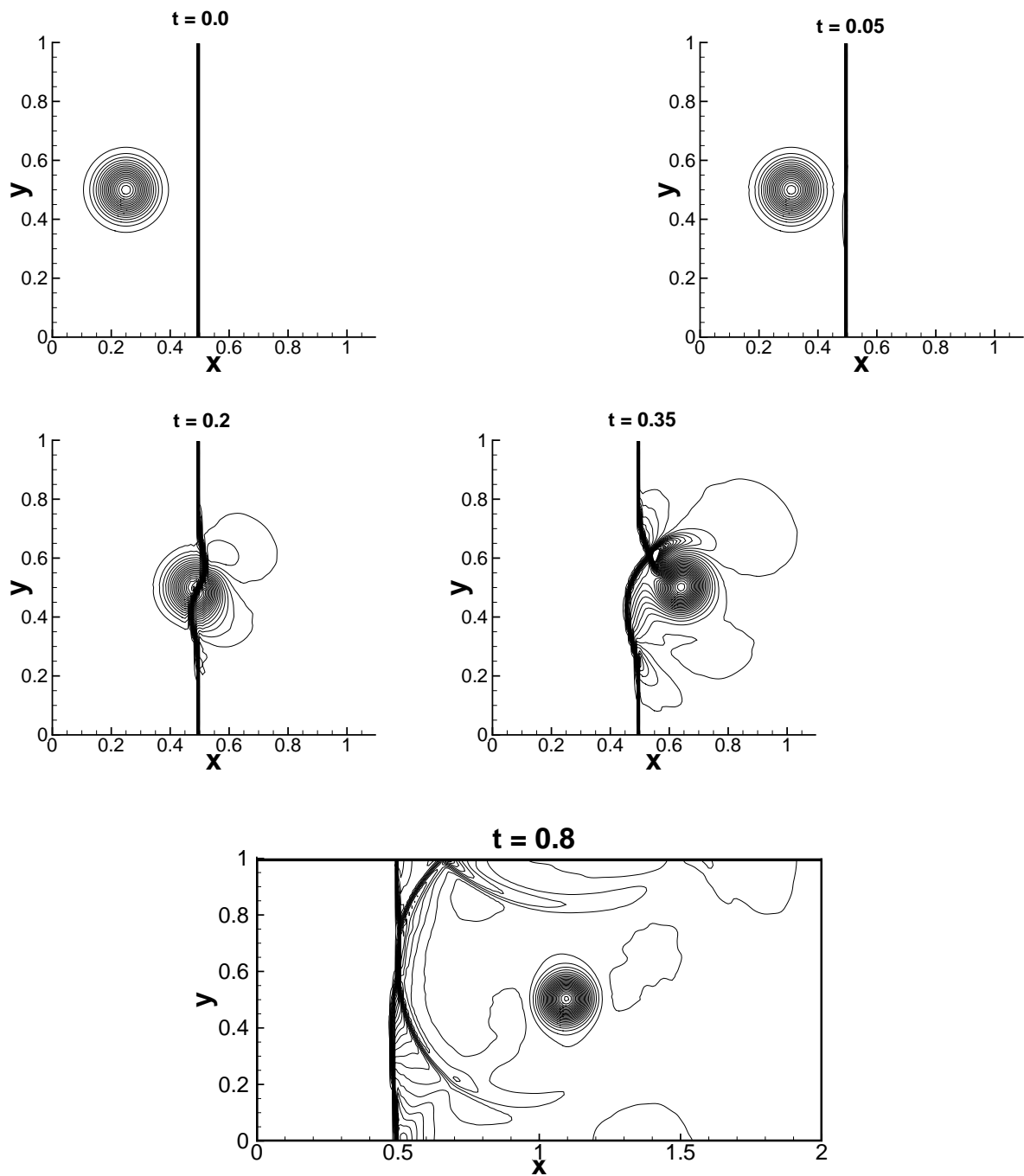


Figure 5: Vortex shock interaction by MPWENO5-GKS. Grid 202×101 , $CFL = 0.1$. Pressure contour at different time, 60 levels between 0.8 and 1.4.

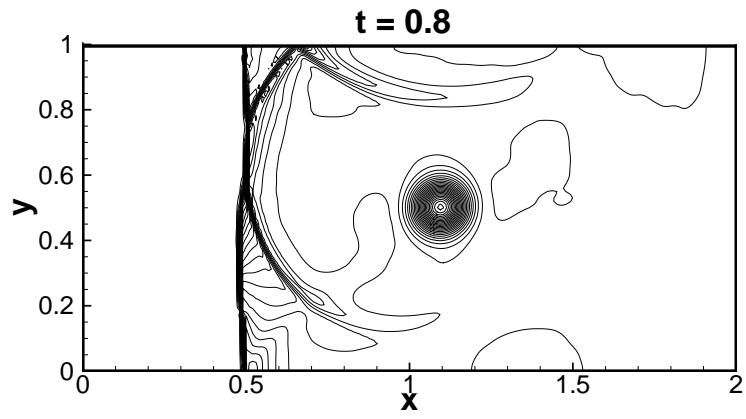


Figure 6: Vortex shock interaction by WENO5-GKS. Grid 202×101 , $CFL = 0.5$. Pressure contour at $t = 0.8$, 60 levels between 0.8 and 1.4.

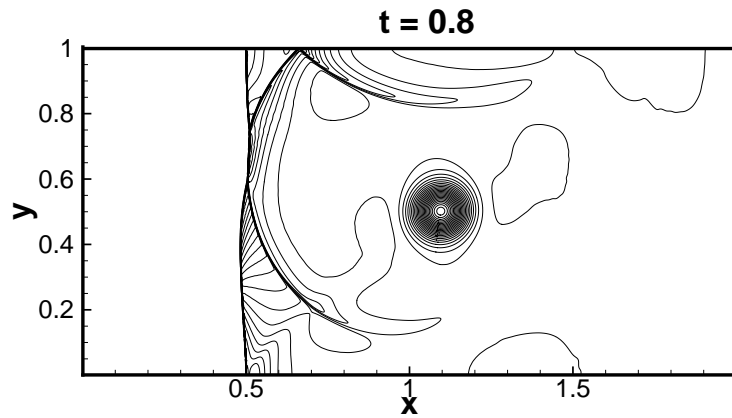


Figure 7: Vortex shock interaction by WENO5-JS. Grid 1202×601 , $CFL = 0.5$. Pressure contour at $t = 0.8$, 60 levels between 0.8 and 1.4.

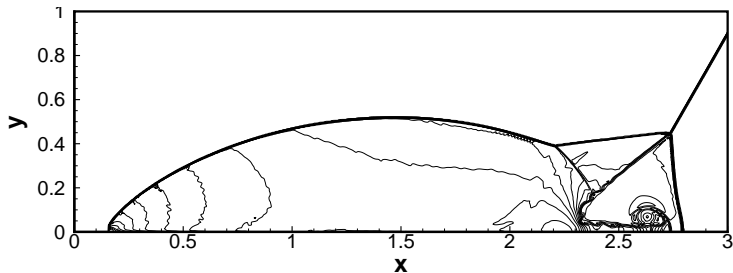


Figure 8: Mach 10 double reflection by MPWENO5-GKS. Grid 960×240 , $CFL = 0.3$. Density contour at $t = 0.2$, 30 levels between 1.5 and 22.7.

point is provided in figure 9. The current results agree well with that in [17], but with a higher resolution.

Example 4.7 Viscous shock tube problem

This is a viscous problem introduced by Daru and Tenaud [4] to test the performances of different schemes. Daru and Tenaud and many other researchers revisited this case later, see Sjögren and Yee [21], Daru and Tenaud [6], et. al. An ideal gas is at rest in a two-dimension box $0 \leq x, y \leq 1$. A membrane with a shock Mach number of 2.37 located at $x = 1/2$ separates two different states of the gas. At time zero the membrane is removed and wave interaction occurs. This is a standard shock tube problem, and would give a familiar one-dimension wave structure if computed by solving a Riemann problem for the inviscid Euler equations. Here, the compressible Navier-Stokes equations with no slip adiabatic boundary conditions are imposed. The solution will develop complex two-dimension shock/shear/boundary-layer interactions, which depend on the Reynolds number. As the Reynolds number increases, the flow structure becomes more complicated.

The dimensionless initial states given in [4] are

$$\rho_L = 120, p_L = 120/\gamma, \rho_R = 1.2, p_R = 1.2/\gamma, \quad (47)$$

where ρ_L, p_L are the density and pressure, respectively, to the left of $x = 1/2$, and ρ_R, p_R are the same quantities to the right of $x = 1/2$. All velocities are zero, $\gamma = 1.4$ and the Prandtl number is 0.73. We compute the case of Reynolds number 1000 to time $t = 1.0$. The velocities and the normal derivative of the temperature at the boundaries are set equal to zero. The computational domain is set to be $(x, y) \in [0, 1] \times [0, 0.5]$. A symmetrical condition is used on the top boundary $x \in [0, 1]$ at $y = 0.5$.

Figure 10 and 11 show the numerical results by MPWENO5- GKS on meshes of 500×250 and 1000×500 grid points, respectively. We can see that the MPWENO5-GKS can effectively capture the interaction of shock wave and boundary layer interactions.

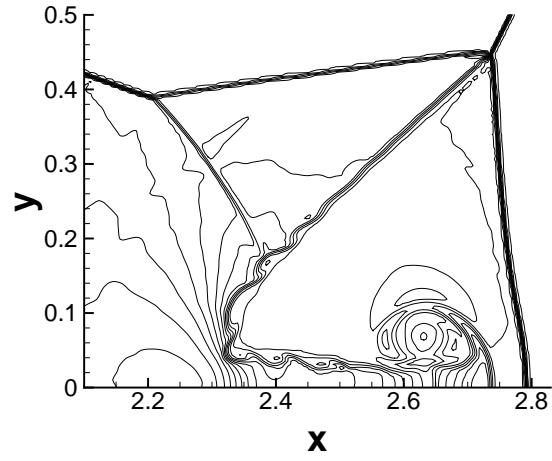


Figure 9: Zoomed-in figure. Mach 10 double reflection. Grid 960×240 , $CFL = 0.3$. Density contour at $t = 0.2$, 30 levels between 1.5 and 22.7.

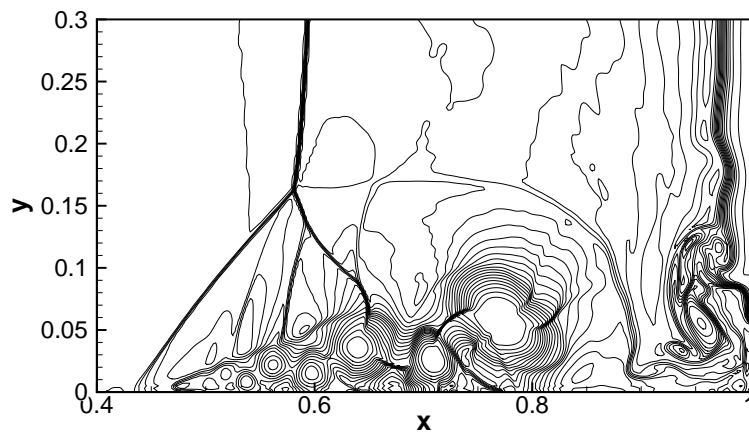


Figure 10: Reflected shock-boundary layer interaction in a shock tube by MPWENO5-GKS. Grid: 500×250 , $CFL = 0.3$, $t = 1.0$. Contour of density, 21 contour levels between 20 and 120.

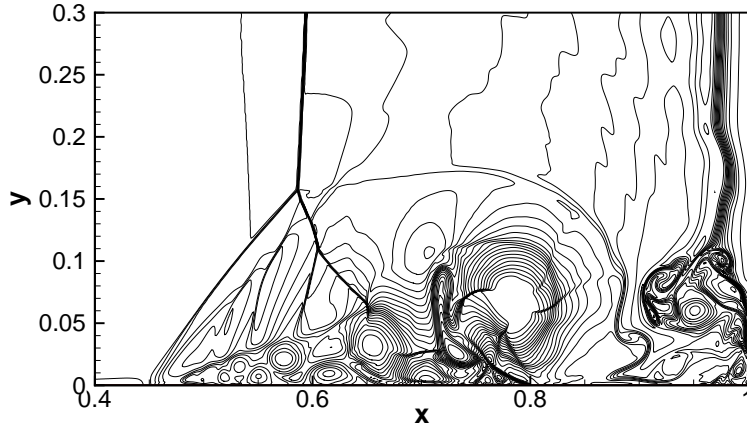


Figure 11: Reflected shock-boundary layer interaction in a shock tube by MPWENO5-GKS. Grid: 1000×500 , $CFL = 0.25$, $t = 1.0$. Contour of density, 21 contour levels between 20 and 120.

6. Conclusion

In this paper, with the enhanced 5th-order WENO interpolation by Yamaleev et. al.'s weight and monotonicity preserving limiter, and with the direct use of the space and time dependent NS gas distribution function, a high order multidimensional finite volume GKS scheme has been constructed. The numerical experiments on one and two dimensional flow problems show that current scheme is a highly efficient and accurate method without numerical oscillations near discontinuity. With the same WENO reconstruction on characteristic variables, the current finite volume gas-kinetic scheme is even more accurate and efficient than the well-defined finite difference WENO-JS method. The current multidimensional scheme can be applied to unstructured mesh as well if initial macroscopic variables with high-order derivatives can be provided at the cell interface.

Besides high-order reconstruction, the success of the WENO5-GKS and MPWENO5-GKS schemes is also due to the coupled space and time evolution of the NS gas distribution function and the multidimensional flux construction. Even with the same accuracy, the absence of Runge-Kutta time stepping makes the current schemes have a shorter stencil than the standard WENO5-JS method. In order to develop a high order scheme with short stencil, we believe that a dynamical model with a nonlinearly coupled spatial and temporal flow evolution at a cell boundary and inside a cell is important, which is to use time accuracy to compensate spatial compactness. The low order dynamics of the Riemann solution is the bottleneck for the further development of high order schemes.

7. Acknowledgments

This work was supported by Hong Kong Research Grant Council (621709, 621011), and HKUST grants SRFI11SC05.

- [1] D.S. BALSARA AND CHI-WANG SHU, *Monotonicity preserving weighted essentially non-oscillatory schemes with increasingly high order of accuracy.*, J. Comput. Phys., 160(2000), pp. 405-452.
- [2] P.L. BHATNAGAR, E.P. GROSS, AND M. KROOK, *A Model for Collision Processes in Gases I: Small Amplitude Processes in Charged and Neutral One-Component Systems*, Phys. Rev., 94 (1954), pp. 511-525.
- [3] J. CASPER, *Finite-volume implementation of high-order essentially non-oscillatory schemes in two dimensions*, AIAA Journal, 30 (1992), pp. 2829-2835.
- [4] V. DARU AND C. TENAUD, *Evaluation of TVD high resolution schemes for unsteady viscous shocked flows.*, Comput. Fluids, 30(2001), pp. 89-113.
- [5] V. DARU AND C. TENAUD, *High order one-step monotonicity-preserving schemes for unsteady compressible flow calculations.*, J. Comput. Phys., 193(2004), pp. 563-594.
- [6] V. DARU AND C. TENAUD, *Numerical simulation of the viscous shock tube problem by using a high resolution monotonicity-preserving scheme.*, J. Comput. Phys., 38 (2009), pp. 664-676.
- [7] Z.L. GUO, H.W. LIU, L.S. LUO, K. XU, *A comparative study of the LBM and GKS methods for 2D near incompressible flows*, J. Comput. Phys. 227 (2008), pp. 4955-4976.
- [8] G.S. JIANG, C.W. SHU, *Efficient implementation of Weighted ENO schemes*, J. Comput. Phys. 126 (1996) 202-228.
- [9] G. KUMAR, S.S. GIRIMAJI, J. KERIMO, *WENO-enhanced gas-kinetic scheme for direct simulations of compressible transition and turbulence*, J. Comput. Phys., in press (2012), <http://dx.doi.org/10.1016/j.jcp.2012.10.005>
- [10] J.Q. LI, Q.B. LI, K. XU, *Comparison of the Generalized Riemann Solver and the Gas-Kinetic Scheme for Inviscid Compressible Flow Simulations*, J. Comput. Phys., 230 (2011), pp. 5080-5099.
- [11] X.D. LIU, S. OSHER, *Weighted essentially non-oscillatory schemes*, J. Comput. Phys., 115 (1994), pp. 200-212.
- [12] Q.B. LI, K. XU, AND S. FU, *A high-order gas-kinetic Navier-Stokes solver*, J. Comput. Phys., 229 (2010), pp. 6715-6731.
- [13] H. W. LIEPMANN, A. ROSHKO, *Elements of Gasdynamics*, Wiley, New York, 1957.
- [14] J. LUO, *A High-order Navier-Stokes Flow Solver and Gravitational System Modeling Based on Gas-kinetic Equation*, PhD Thesis, Hong Kong University of Science and Technology (2012).

- [15] T. OHWADA AND K. XU, *The kinetic scheme for full Burnett equations*, *J. Comput. Phys.* **201** (2004), pp. 315-332.
- [16] T. OHWADA AND S. FUKATA, *Simple derivation of high-resolution schemes for compressible flows by kinetic approach*, *J. Comput. Phys.* **211** (2006), pp. 424.
- [17] J. QIU AND C.-W. SHU, *Finite difference WENO schemes with Lax-Wendroff type time discretizations*, *SIAM Journal on Scientific Computing*, 24 (2003), pp. 2185-2198.
- [18] C.W. SHU AND S. OSHER, *Efficient implementation of essentially nonoscillatory shock-capturing schemes II*, *J. Comput. Phys.*, 83 (1989), pp. 32-78.
- [19] C.W. SHU, *Essentially non-oscillatory and weighted essentially non-oscillatory schemes for hyperbolic conservation laws*, *Lecture Notes in Mathematics*, Springer, 1998.
- [20] A. SURESH AND H.T. HUYNH, *Accurate monotonicity-preserving schemes with Runge-Kutta time stepping.*, *J. Comput. Phys.*, 136 (1997), pp. 83-99.
- [21] B. SJÖGREEN AND H. C. YEE, *Grid convergence of high order methods for multiscale complex unsteady viscous compressible flows.*, *J. Comput. Phys.*, 185 (2003), pp. 1-26.
- [22] P. WOODWARD AND P. COLELLA, *Numerical simulations of two-dimensional fluid flow with strong shocks*, *J. Comput. Phys.*, 54 (1984), pp. 115-173.
- [23] K. XU, *Gas-Kinetic Schemes for Unsteady Compressible Flow Simulations*, von Karman Institute report, (1998-03).
- [24] K. XU, *A gas-kinetic BGK scheme for the Navier-Stokes equations, and its connection with artificial dissipation and Godunov method*, *J. Comput. Phys.*, 171 (2001), pp. 289-335.
- [25] K. XU AND X.Y. HE, *Lattice Boltzmann method and Gas-kinetic BGK scheme in the low Mach number viscous flow simulations*, *J. Comput. Phys.*, 203 (2005), pp. 100-117.
- [26] K. XU, M.L. MAO, AND L. TANG, *A multidimensional gas-kinetic BGK scheme for hypersonic viscous flow*, *J. Comput. Phys.*, 203 (2005), pp. 405-421.
- [27] L.J. XUAN AND K. XU, *A new gas-kinetic scheme based on analytical solutions of the BGK equation*, *J. Comput. Phys.*, in press (2012), <http://dx.doi.org/10.1016/j.jcp.2012.10.007>
- [28] N. K. YAMALEEV, M. H. CARPENTER, *A systematic methodology for constructin high-order energy stable WENO schemes*, *J. Comput. Phys.*, 228 (2009), pp. 4248-4272.